

# Investigation of *veryintenseD3*-band emission in multi-crystalline silicon wafers using electron microscopy and hyperspectral photoluminescence imaging

Cite as: J. Appl. Phys. **131**, 145703 (2022); <https://doi.org/10.1063/5.0087119>

Submitted: 01 February 2022 • Accepted: 25 March 2022 • Published Online: 12 April 2022

 Annett Thøgersen, Ingvild J. T. Jensen,  Joachim S. Graff, et al.




View Online




Export Citation



CrossMark






## Instruments for Advanced Science

- Knowledge,
- Experience,
- Expertise


Click to view our product catalogue

Contact Hiden Analytical for further details:  
[www.HidenAnalytical.com](http://www.HidenAnalytical.com)  
[info@hideninc.com](mailto:info@hideninc.com)




Gas Analysis

- ▶ dynamic measurement of reaction gas streams
- ▶ catalysis and thermal analysis
- ▶ molecular beam studies
- ▶ dissolved species probes
- ▶ fermentation, environmental and ecological studies




Surface Science

- ▶ UHVTPD
- ▶ SIMS
- ▶ end point detection in ion beam etch
- ▶ elemental imaging - surface mapping



Plasma Diagnostics

- ▶ plasma source characterization
- ▶ etch and deposition process reaction kinetic studies
- ▶ analysis of neutral and radical species



Vacuum Analysis

- ▶ partial pressure measurement and control of process gases
- ▶ reactive sputter process control
- ▶ vacuum diagnostics
- ▶ vacuum coating process monitoring



# Investigation of *veryintenseD3*-band emission in multi-crystalline silicon wafers using electron microscopy and hyperspectral photoluminescence imaging

Cite as: J. Appl. Phys. **131**, 145703 (2022); doi: [10.1063/5.0087119](https://doi.org/10.1063/5.0087119)

Submitted: 1 February 2022 · Accepted: 25 March 2022 ·

Published Online: 12 April 2022





View Online



Export Citation



CrossMark

Annett Thøgersen,<sup>1,a)</sup>  Ingvild J. T. Jensen,<sup>1</sup> Joachim S. Graff,<sup>1</sup>  Inga Gudem Ringdalen,<sup>2</sup>  
Patricia Almeida Carvalho,<sup>1</sup> Torbjørn Mehl,<sup>3</sup>  Junjie Zhu,<sup>4</sup> Ingunn Burud,<sup>3</sup> Espen Olsen,<sup>3</sup> and Rune Søndena<sup>4</sup> 

## AFFILIATIONS

<sup>1</sup>SINTEF, Materials Physics, Forskningsveien 1, 0373 Oslo, Norway

<sup>2</sup>SINTEF, Materials Physics, Høgskoleringen 5, 7034 Trondheim, Norway

<sup>3</sup>Norwegian University of Life Sciences (NMBU), Institute of Physics, Universitetstunet 3, 1433 Ås, Norway

<sup>4</sup>Institute for Energy Technology, Department of Solar Energy, Instituttveien 18, 2007 Kjeller, Norway

<sup>a)</sup>Author to whom correspondence should be addressed: [annett.thogersen@sintef.no](mailto:annett.thogersen@sintef.no)

## ABSTRACT

Defects in high performance multi-crystalline silicon wafers can be detrimental to the lifetime of the solar cell. It is, therefore, important to study and understand the underlying structure and chemical elements present at these defective areas in order to suppress them. The underlying cause of the D-band emission line “*veryintenseD3*” (VID3) has not yet been understood, although many theories have been proposed. In this paper, we have investigated the underlying causes of the d-band emission peak VID3 by hyperspectral photoluminescence imaging, scanning electron microscopy, electron backscatter diffraction, scanning transmission electron microscopy, and density functional theory (DFT) to understand the defect structure in areas of a VID3 emission peak in more detail. We found a high VID3 peak intensity at sub-grain and  $\Sigma 3$  twin boundaries bordering to grains with a small misorientation, which suggests higher stress in these regions. Defects close to the twin boundary indicate a light element dopant in the area, such as oxygen. DFT calculations show that oxygen is prone to segregate to this boundary.

© 2022 Author(s). All article content, except where otherwise noted, is licensed under a Creative Commons Attribution (CC BY) license (<http://creativecommons.org/licenses/by/4.0/>). <https://doi.org/10.1063/5.0087119>

## I. INTRODUCTION

High performance multi-crystalline (hpmc) silicon contains dislocations and grain boundaries introduced during the solidification process, in addition to impurities in-diffused from the crucible.<sup>1</sup> Material defects, such as dislocations, grain boundaries, and impurities, can act as recombination centers for electrons and holes, thereby reducing the carrier lifetime of silicon wafers for photovoltaic (PV) applications. Hydrogen can bond with and passivate a wide range of these defects and impurities in silicon.<sup>2–8</sup> Thus, hydrogenation is an important step for improving the performance of crystalline silicon solar cells. It is especially important in multicrystalline silicon wafers due to its content of extended crystal

defects, such as grain boundaries (GBs) and dislocation clusters. However, not all extended defects respond equally well to the hydrogenation process. Dislocation clusters rarely improve, while hydrogenation generally passivates GBs. However, not all grain boundaries are passivated during hydrogenation; small-angle, random-angle, and some cases of coincidence site lattice (CSL) grain boundaries remain recombination active even after hydrogenation.<sup>9</sup> It is, therefore, important to understand the nature of the material structure and interfaces of the grain boundaries and defects. A better understanding of the mechanism behind hydrogen passivation of extended defects may result in optimized processes and increased performance of solar cells.

D-band emission lines were first described by Drozdov and Partin<sup>10</sup> in 1976. These lines were reported as emissions due to (or associated with) dislocations in silicon.<sup>10,11</sup> The D-lines have been labeled D1 for the 0.812 eV peak, D2 for 0.875 eV, D3 for 0.934 eV, and D4 for 1.000 eV.<sup>10–13</sup> The D1 and D2 lines have often been reported to originate from point defects located in the elastic strain field around dislocations,<sup>12,14</sup> the so-called Cottrell atmospheres. Since the emission peak of D3 and D4 is mainly confined to dislocation cores or sub-GBs, it has often been assumed to be due to the defects themselves.<sup>12,15–17</sup> However, the D3 emission has also been correlated with oxygen precipitates<sup>18</sup> and metal iron impurities.<sup>19</sup> On the other hand, Wyller *et al.*<sup>14</sup> found that in regions with high concentration of iron precipitates, the D3 and D4 emissions were reduced, while Nguyen *et al.*<sup>20</sup> found no effect on the D3 and D4 emission by iron precipitates. Although no clear consensus has been found on the exact underlying causes of the D3 and D4 peak, they are generally understood to be correlated to the same defect.<sup>21</sup> In addition, a sharp peak emission at 0.934 eV is often found to be at similar energy as D3, but with different peak energy distribution and properties.<sup>1</sup> This peak is called “*veryintenseD3*” (VID3). To best image this peak separately from D4, an image showing the difference between D4 and D3 has been reported.<sup>1</sup>

During crystal growth, large angle grain boundaries can act as relaxation points for stress and strain.<sup>17</sup> This can reduce the dislocation density in the nearby regions. Small-angle grain boundaries (sub-grain boundaries) on the other hand can be a result of high stress exposure within a grain. These sub-grain boundaries are, therefore, often found in areas of high defect density and can trap other defects and impurities and become recombination active. Nguyen *et al.*<sup>17</sup> reported that the sub-GBs that only emit D3/D4 peaks may contain dislocations and stacking faults, but that a more detailed microscopic structure study combined with high spatial resolution photoluminescence (PL) spectroscopy maps need to be carried out to confirm the hypothesis. We have, therefore, focused on investigating areas in the wafer-sample with high D-band emission lines VID3 (0.934 eV) using hyperspectral PL (HSPL), scanning electron microscopy (SEM), electron backscatter diffraction (EBSD), scanning transmission electron microscopy (STEM), as well as modeled the grain boundaries and atom segregation using density functional theory (DFT).

## II. METHODS

In this study, commercially available boron doped hpmc Si wafers with a resistivity of approximately 1 Ω cm were investigated. As-sawn wafers were damage etched in a HNA-solution (HF, nitric acid, acetic acid) before in-diffusion of a two-sided phosphorus emitter ( $\approx 70 \Omega/\text{sq.}$ ) in a POCl<sub>3</sub> tube-furnace.<sup>22</sup> A hydrogen-rich SiN<sub>x</sub> anti-reflective coating (ARC) was deposited on both sides of the wafers prior to a simulated contact firing process (without the metal contacts present) in a belt furnace. The ARC and the phosphorus emitter layers were then removed in a new HNA-solution. Hydrogenation of the wafers using this process routine has been confirmed using FT-IR (Weiser *et al.*<sup>23</sup>). The wafers were then cleaned and surface passivated using an *a*-Si:H/SiN<sub>x</sub>:H-stack deposited by plasma-enhanced chemical vapor deposition. Surface recombination velocities of less than 5 cm/s are routinely obtained

using this process.<sup>24</sup> Hyperspectral photoluminescence (HSPL) images, of samples cooled with liquid nitrogen to 90 K, were obtained by using a NIR hyperspectral pushbroom camera (SWIR, Specim, Finland). A similar setup has been used in previous studies.<sup>25,26</sup> To separate the signals found in specific areas of the sample, multivariate curve resolution (MCR)<sup>27</sup> analysis was conducted on the hyperspectral image. In order to understand and correlate the material properties with a specific spectral photoluminescence (HSPL) peak, we have used electron backscattered diffraction (EBSD) in the scanning electron microscope (SEM) to study the type of grain boundary and defect that resulted in a specific D-band emission line. We have then used focused ion beam (FIB) with Ga<sup>+</sup> ions accelerated at 30 kV using a JEOL JIB 4500 multibeam system to prepare samples from selected regions of interest for scanning transmission electron microscopy (STEM). Analysis of the atomic and electronic structure was carried out using a DCOR Cs probe-corrected FEI Titan G2 60-300 microscope with 0.08 nm of nominal spatial resolution, a Bruker super EDX detector, and a GIF Quantum 965 EELS Spectrometer using annular bright-field (ABF), low-angle annular dark field (ADF), and high-angle annular dark field (HAADF) STEM detectors. The structure of the silicon was indexed using fast Fourier transform (FFT), and the strain was evaluated by geometric phase analysis (GPA) using the FRWRtools plugin<sup>28</sup> implemented in Digital Micrograph (Gatan, Inc).

Density functional theory (DFT) simulations were performed using the Vienna *ab initio* simulation package (VASP).<sup>29,30</sup> The Perdew–Burke–Ernzerhof (PBE) generalized gradient approximation (GGA)<sup>31</sup> functional was used. A convergence criterion in the change of the total energy of less than 10<sup>−5</sup> eV was used for the ionic relaxations. The plane-wave energy cut-off used was 420 eV. A gamma sampling of 0.25 *k*-points per Å was used for the Brillouin zone.

The segregation energies ( $\Delta E_X$ ) were calculated from

$$\Delta E_X = (E_X - E_{ref}) - (E_{bulkX} - E_{bulkSi}), \quad (1)$$

where  $E_X$  is the energy of the twin boundary with solute,  $E_{ref}$  is the energy of the twin boundary with only Si,  $E_{bulkX}$  is the energy of one solute atom in bulk Si, and  $E_{bulkSi}$  is the energy of one Si atom in bulk Si.

## III. RESULTS

Figure 1 shows an optical image of the Si-wafer with overlaid HSPL peak intensity maps (the VID3 peak is in yellow). The contrast generated revealed a microstructure of coarse polygonal grains, often displaying characteristic growth twins. No apparent relation between specific micro-structural features and PL emission could be identified at this scale. Two areas (Areas A and B in Fig. 1) have been selected to be further scrutinized in detail. These areas emitted only in the VID3 band spectral range and from projected long slices, and these areas are easier to identify in the SEM. A PL spectrum containing the VID3 band emission peak from this area can be seen in Fig. 2 together with a PL spectrum in an area with no defects. The VID3 peak is located at 0.934 eV, while the peak at 1.1 eV is the band-to-band emission peak.

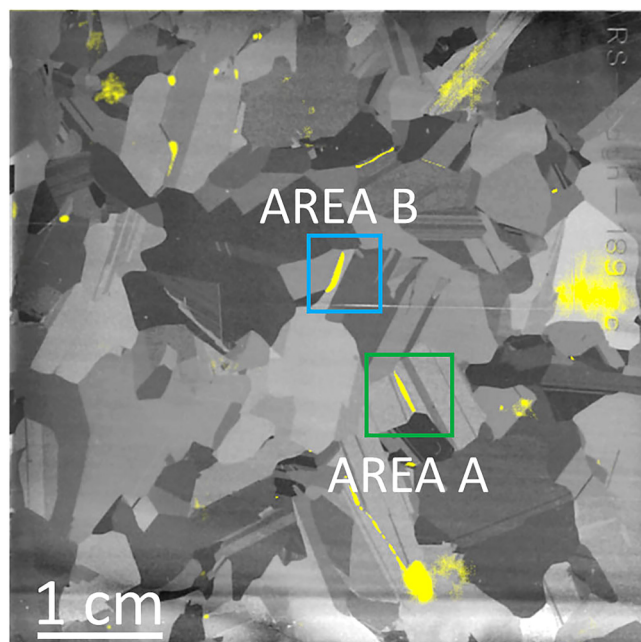


FIG. 1. Optical image of the wafer with HSPL intensities for VID3 in yellow showing the two areas investigated in this paper (Areas A and B).

Area A was then investigated further with SEM and EBSD. Figures 3(a) and 3(b) show an optical image and an SEM band contrast image with PL intensity overlaid. Here, we can observe the location of the possible grain boundary (GB) that exhibits the HSPL-VID3 band emission. The SEM image shows more detail of the GB and the location of the areas investigated with TEM. Figure 3(c) shows an EBSD image of the grain orientations and the type of GBs present at the HSPL emission area and in the surrounding areas. The map shows many  $\Sigma 3$  GBs with an active slip

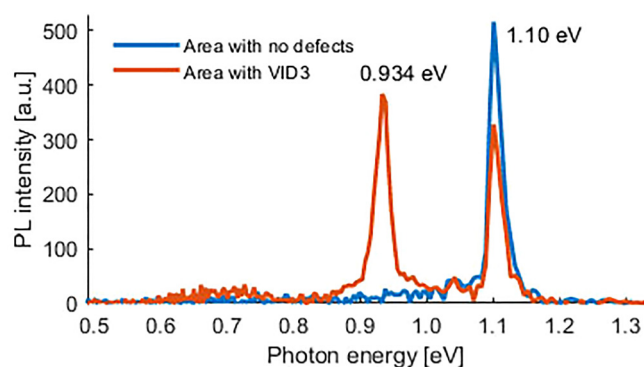


FIG. 2. Photoluminescence spectra showing the VID3 band emission peak (at 0.934 eV) mapped in Fig. 1 together with the band-to-band peak (at 1.1 eV) in areas with no defect.

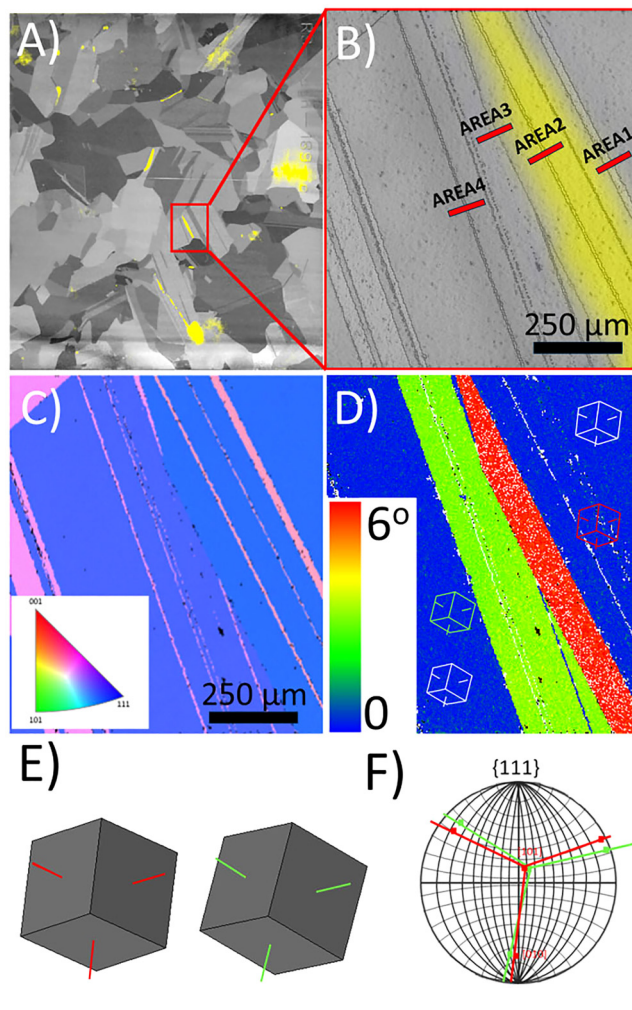
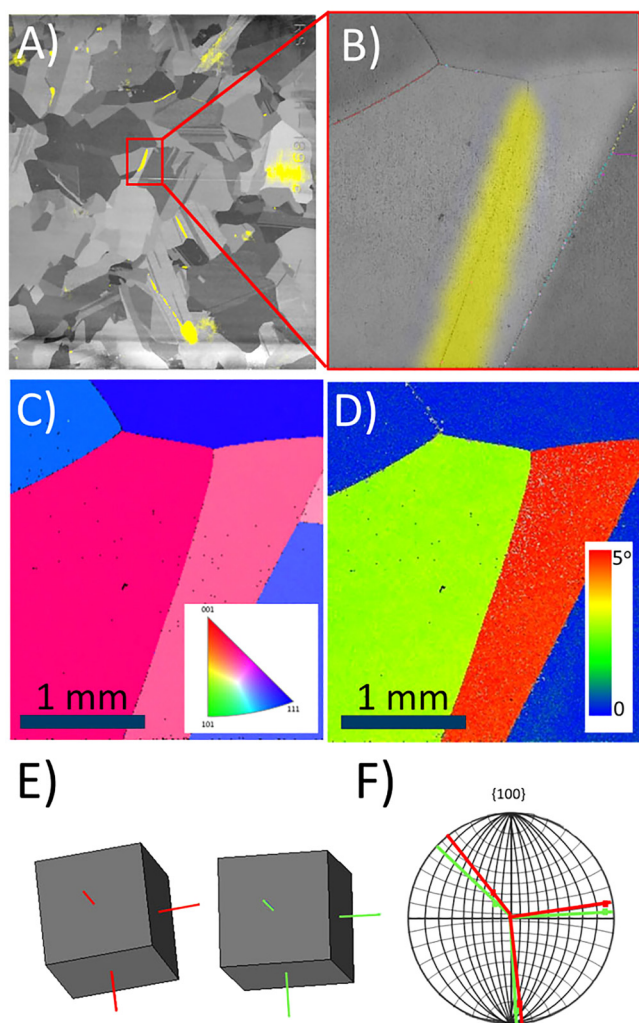


FIG. 3. Area A: (a) optical image with HSPL image overlaid, (b) a band contrast image with HSPL image overlaid [with the location of FIB samples (Area 1–Area 4)], (c) an EBSD image (grain orientation) showing many  $\Sigma 3$  twin boundaries with the active slip system  $\{1 - 10\}\{111\}$ , (d) a grain orientation deviation map with the oriented structures as an inset, (e) a crystal orientation of the green and red grain in (d), and (f) a stereographic projection of the 111 with points and orientations of the two crystals in (e).

system  $\{1 - 10\}\{111\}$ . The GBs in the HSPL intensity center are  $\Sigma 3$  twin boundaries. However, there are many other  $\Sigma 3$  GBs in the surrounding area that do not exhibit the VID3 band emission character. We have, therefore, selected four areas of interest to examine further with TEM, one without the VID3 band emission peak, two on the edge of the signal, and one in the center of the signal [as shown in Fig. 3(b)]. Figure 3(d) shows a grain reference orientation deviation (GROD) angle from the same area. This is the mean misorientation of each pixel relative to the mean orientation of all points belonging to the area.<sup>32</sup> The HSPL VID3 band emission area is located in an area with a  $5^\circ$  misorientation angle, relative to the mean orientation of the grain. The neighboring area has a GROD

angle of  $2.5^\circ$ . This shows that this area has undergone more strain than the surrounding areas with assumed similar types of GBs. The structural orientation of the different grain is shown as an inset in the image. The orientation of the green and red grain in Fig. 3(d) is shown in (e), and their orientation relationship can be seen from the stereographic projection in Fig. 3(f). Tilted about  $20^\circ$  with respect to the surface normal of the 111 plane, the two orientations have a similar  $\langle 110 \rangle$  tilt axis.

The VID3-band emission intensity can also be observed in Area B, shown in Fig. 4(a) and more closely in the EBSD-SEM band contrast image in Fig. 4(b). The HSPL-VID3 band emission



**FIG. 4.** Area B: (a) optical image with HSPL image overlaid, (b) a band contrast image with HSPL image overlaid, (c) an EBSD grain orientation image [inverse pole figure (IPF) in the Z direction] showing a sub-grain boundary, (d) a grain reference orientation deviation (GROD) angle map, (e) a crystal orientation of the green and red grain in (d), and (f) a stereographic projection of the 111 with points and orientations of the two crystals in (e).

peak is located on a sub-grain boundary, with only about a  $\sim 10^\circ$  tilt difference, shown in the EBSD grain orientation image in Fig. 4(c). A FIB sample was made from the sub-grain, but the grain boundary was not observable. The grain reference orientation deviation angle map of Area B is shown in Fig. 4(d). As seen in Area A, the area of high HSPL-VID3 intensity is from an area with a  $\sim 5^\circ$  GROD angle with a boundary to a grain with a  $\sim 3^\circ$  GROD angle. The structural orientation of the different grain is shown as an inset in the image. The orientation of the green and red grain in Fig. 3(d) is shown in (e), and their orientation relationship can be seen from the stereographic projection in Fig. 3(g).

High resolution STEM (HAADF) images of Area 1, Area 2, and Area 4 in Area A is shown in Fig. 5. These three areas are from the edge of the signal (Area 1), the center of the signal (Area 2), and the area with no signal (Area 4). The images all show grain boundaries containing coherent  $\Sigma 3_{\{111\}}$  twin boundaries. We found an angle of  $\sim 143^\circ$  between all the twin plane (half of that is  $\Theta = 71.5^\circ$ ); this is slightly higher than  $\Theta_{\Sigma 3}$  of  $70.5^\circ$  defined by the

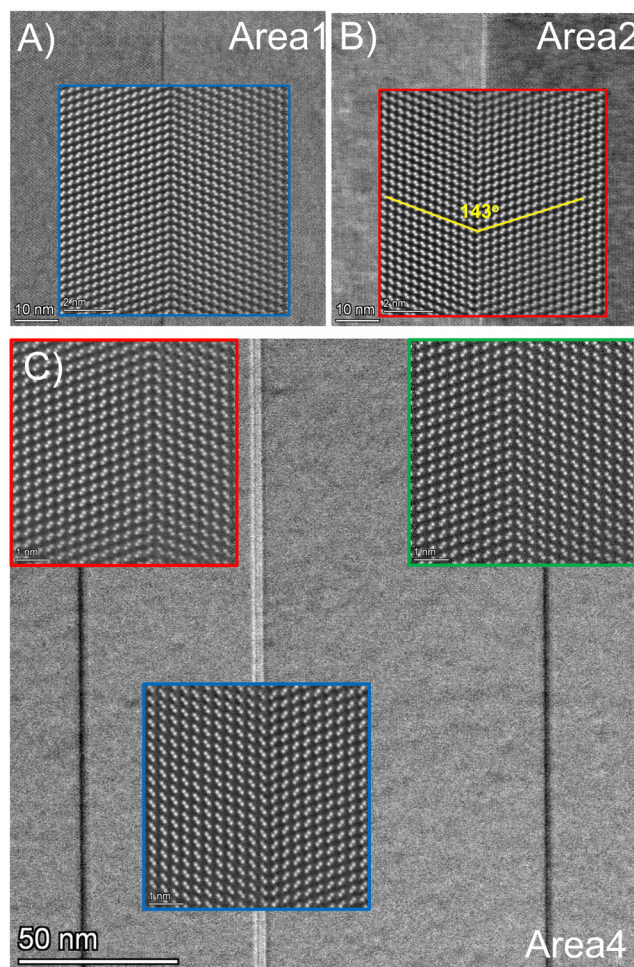


**FIG. 5.** High resolution STEM images of (a) Area 1, (b) Area 2, and (c) Area 4.

coincidence site lattice (CSL) relation.<sup>33,34</sup> No other defects or precipitates were found in or near the twin boundary.

High resolution STEM images of Area 3 (Fig. 6) show the same type of  $\Sigma 3_{\{111\}}$  twin boundary as found for the other areas in

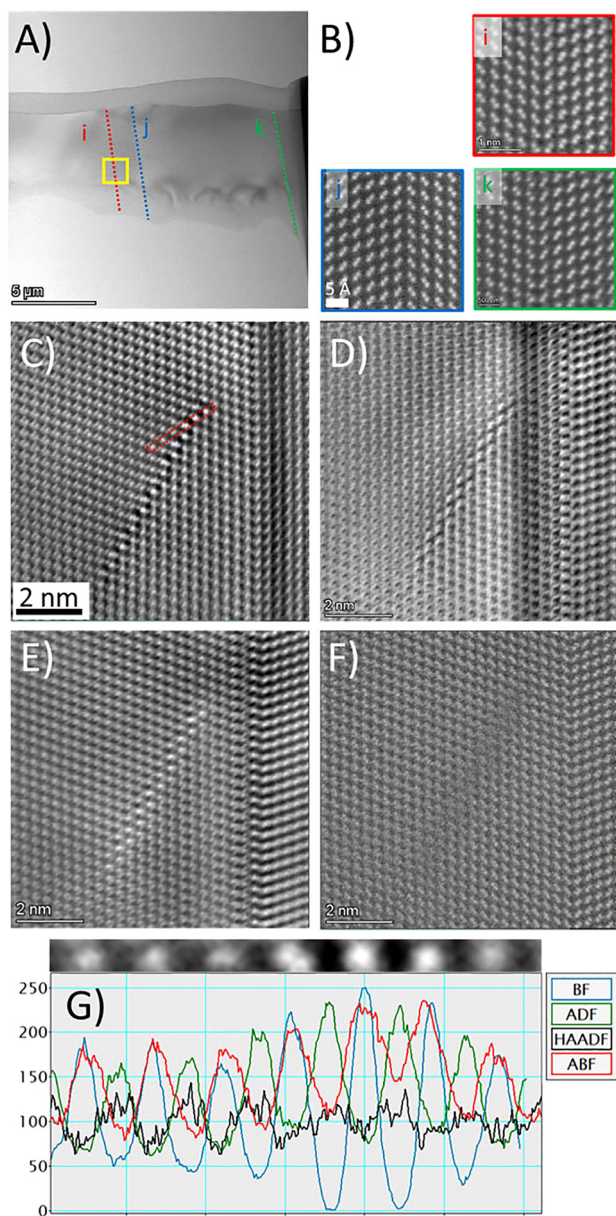


**FIG. 6.** (a) STEM image of Area 3 showing three twin grain boundaries (i)–(k) and the yellow square marks of defect in (c)–(g). (b) HR-STEM images of the twin boundaries in (a). (c) BF-STEM, (d) ABF-STEM, (e) ADF-STEM, (f) HAADF-STEM image of the defect, and (g) presents an intensity contrast from the red square in figure (a) from detector BF, ABF, ADF, and HAADF in the defect region, with the BF image of the area investigated on top.

Fig. 5. However, when we take a closer look at one of the twin boundaries in Fig. 6 boundary i [location shown by the yellow square in Fig. 6(a)], a small defect close to the twin boundary can be seen, and the area is presented in Figs. 6(c)–6(g). The habit plane of the defect seems to be 113. Figures 6(c)–6(f) show the bright-field (BF), annular BF (ABF), the annular dark field (ADF), and high angled annular DF (HAADF) detectors found with a camera length of 48 mm. The defect has a bright contrast in ABF and ADF detector images indicating small strain. The HAADF detector image, which would show a difference in atomic weight, on the other hand, does not show this defect. However, the image signal is slightly weak in this area. The contrast intensity at the defect [the red square in Fig. 6(c), as well as for all the detector images] is plotted in Fig. 6(g), with the BF image investigated on top. In the BF image, the dark areas are the atomic columns and the bright areas holes/lighter elements. The plot shows low intensity of the HAADF detector, while the ABF detector shows a more broad peak intensity in between the atomic columns (especially in the middle of the two high contrast BF peaks). This shows high intensity at low collection angles/low scattering.

To investigate this defect further, geometric phase analysis (GPA) of the bright-field (BF) image was carried out using the (220) reflection to study if the contrast variations resulted from strain from the area in Figs. 6(c)–6(g); see Fig. 7(a). The GPA shows an area of only very small compressive and tensile strain (less than 1%), shown in Fig. 7(b). This may be too small strain for this to be due to dislocations or stacking faults and may be more likely due to substitutional elements. Since the HAADF image shows less intensity in this area, we may have the presence of a lighter element, such as O, B, N, C, or O–H complex. Figure 7(c) shows an image made by first masking in all diffraction points related to the 110 projection in a fast Fourier transformed image (FFT) and then making an image by inverse FFT only these diffraction points. The blue and green square shows an area of the sample that has been used for the FFT patterns in (e) and (f). However, the actual analysis area is much bigger. Figure 7(d) is made by making an image from what is left after removing all diffraction points. The structure above and below the defect seems slightly tilted. Figure 6(e) shows the FFT pattern of the structure below the defect, while Fig. 6(f) from above the defect. Red arrows in the image are indicating diffraction spots that have an increased intensity in the area above the defect. Simulated diffraction images using JEMS-SWISS<sup>35</sup> of the pristine Si structure in the [110] projection and in the tilted projection are shown in Figs. 6(g) and 6(h), respectively. The Si crystal above the defects seems to be tilted in the [1–1–1] direction, where the center of the Laue circle is at around (7.0, –7.0, –4.7). This seems to either be a small defect or a sub-grain boundary extending from the twin.

Impurity segregation to the  $\Sigma 3_{\{111\}}$  grain boundary was calculated with DFT for light element impurities, such as boron, nitrogen, and carbon. The results are shown in Fig. 8. When incorporating an impurity atom into the twin boundary (in various atomic configurations), the segregation energy shows the most stable positions when negative. From these calculations, it seems that N is most favorable for segregating toward the  $\Sigma 3_{\{111\}}$  grain boundary. Carbon on the other hand has the least favorable segregation energies and will tend to rather diffuse in bulk than to the

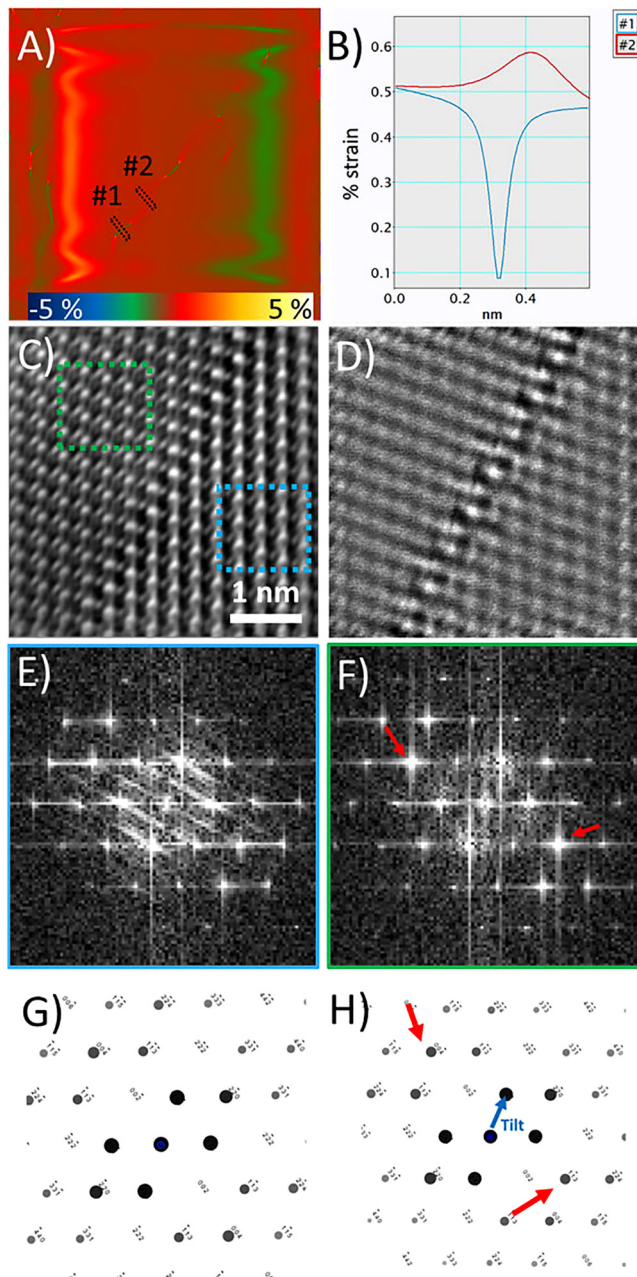


**FIG. 7.** (a) GPA map of image (a) in Fig. 6(a) using  $d_{220}$  reflection, (b) shows strain intensity in the defected regions shown in (a), (c) a filtered image, of a higher resolution image, using all diffraction spots related to the 110 projection [blue and green squares indicate a part of the sample used for FFT (the actual area is much bigger)], (d) a filtered image using what was not imaged in (c), (e) the FFT pattern of the area above the defect, (f) the FFT pattern of the area below the defect [red arrows indicate an increased intensity in the (113) spot], (g) a simulated electron diffraction pattern of a pristine Si crystal in [110] projection, and (h) a Simulated electron diffraction pattern of an Si crystal tilted in the  $[1-1-1]$  direction where the center of the Laue circle is at  $(7.0, -7.0, -4.7)$ .

twin boundaries. However, in these calculations, we have only considered substitutional segregation. However, for the lighter elements, the diffusion process may be more complicated because interstitial segregation is a possibility and may be more favorable.<sup>36</sup>

#### IV. DISCUSSION

In summary of the two areas investigated, we found

1. Area A:
  - (a) Contained many coherent  $\Sigma 3_{\{111\}}$  grain boundaries.
  - (b) Some of the GB-areas are recombination active and some are not.
  - (c) High grain reference orientation angle (high stress) in surrounding grains to boundary with high VID3 emission.
  - (d) Defect/impurity found in a VID3/high GROD-region.
2. Area B:
  - (a) Sub-grain/small-angle GB.
  - (b) High GROD angle.
3. Modeling:
  - (a) The most probable element for substitutional segregation to the twin boundary is oxygen.

Both areas (Areas A and B) with a high HSPL VID3 band emission peak shows high GROD intensity (high misorientation angle) compared to the surrounding areas. In both areas, the intensity is at a boundary between two grains or areas in between twin planes that both have a GROD misorientation angle of  $5^\circ$  and the other with  $2^\circ-3^\circ$ . This misorientation shows strain that could have been caused by the crystal growth or possibly by impurities and defects in the structure. The stereographic projection in Fig. 3(f) of Area A shows that the two grains have a common tilt axis, the  $\langle 110 \rangle$ . We can, therefore, assume that most of the misorientation around the  $\Sigma 3$  GBs are due to a tilt around this axis. Any misfit dislocations will extend along this axis, which is almost parallel to the FIB sample and will, therefore, be difficult to observe.

All grain boundaries in Area A consist of coherent  $\Sigma 3$  twin boundaries. These types of twin boundaries are very common in photovoltaic multicrystalline silicon (mc-Si).<sup>37-39</sup> Defect free coherent  $\Sigma 3$  twin boundaries are found to have very low boundary energy, negligible electrical activity, and recombination free.<sup>33,37,40,41</sup> They, therefore, present very little damage to the electrical properties of the wafer and can be beneficial to the overall solar cell device due to the improved minority carrier diffusion lengths. However, if the  $\Sigma 3$  twin boundary is incoherent or decorated with dislocations or metallic impurities, the twin boundary will have an increased electrical activity and the minority carrier diffusion length will be considerably reduced.<sup>33,37,42-45</sup> The  $\Sigma 3$  twin boundary has generally a  $140.5^\circ$  misorientation angle between the (111) planes, which gives an  $\theta_{\Sigma 3}$  ( $70.5^\circ$ ) of half, which is defined by the coincidence site lattice (CSL) relation.<sup>33</sup> Ohno *et al.*<sup>45</sup> found high recombination activity in twin boundaries with a positive deviation in the tilt angle  $\theta_{\Sigma 3} > 70.5^\circ$ . In addition, if these boundaries are less harmful to the photoelectric properties, they can also result in  $\Sigma 9$  and  $\Sigma 27$  boundaries, which are more recombination active and may contain precipitates, such as Fe, C, or O.<sup>37,46</sup> However, none of these have been observed. Electrical activity of defects may be due to minority carrier trapping levels present in

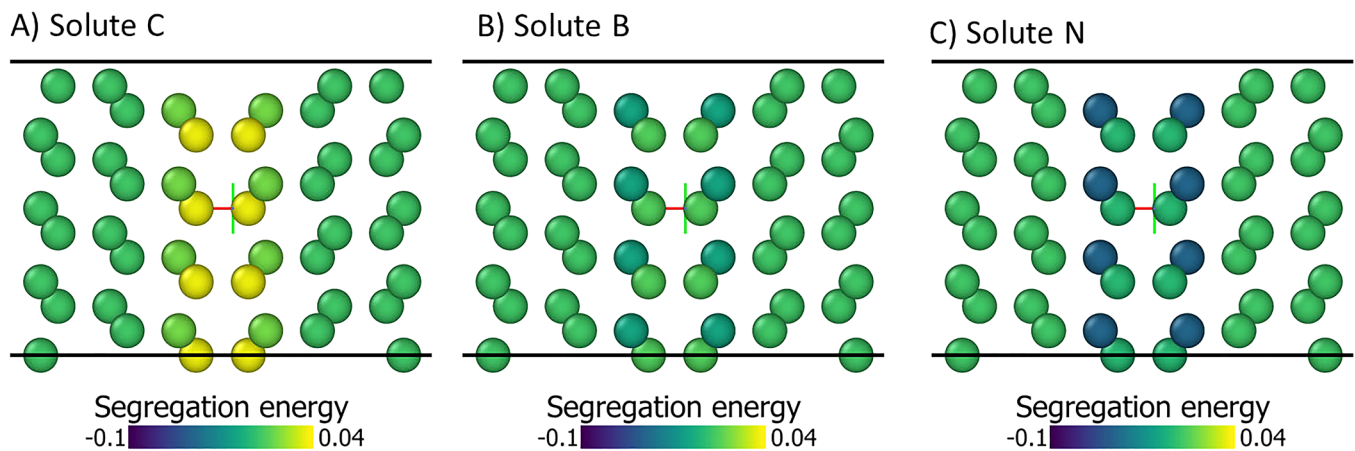


FIG. 8. Segregation energy at a twin boundary found by DFT for impurity: (a) carbon, (b) boron, and (c) nitrogen.

the bandgap, which are acting as recombination centers,<sup>47</sup> such as dangling bonds.<sup>41</sup> If the symmetry of the  $\Sigma 3$  twin boundary is partly broken, the grain boundary may become electrically active.<sup>33</sup> The twin boundaries observed in this sample were all with a  $\theta_{\Sigma 3} = 71.5^\circ$ . However, they all seem to be coherent twin boundaries. No defects seem to have been connected to the twins, part from the small defect observed in Fig. 6. There could be defects in other planes not observed in our analysis.

The sub-grain boundary in Fig. 4 of Area B shows a small tilt between the two grains, and no sectioning of the grain boundary has been observed but may exist. Sub-grain boundaries have been reported to behave as shunts, with increased electrical activity, and are strong recombination sites for minority carriers compared to random GBs.<sup>48</sup> In order to improve the overall performance of an Si solar cell, this defect should be avoided.

In a previous study on boron (B) doped cubic silicon carbide (SiC),<sup>49</sup> we observed an atomic layer of B in the SiC structure by STEM and GPA analysis. Boron is a light material and will scatter in low angles in the TEM. Using low collection angles to observe them was important. Boron had also only a small effect on the high-angle annular dark field STEM image. This is similar to what we can observe in our HRSTEM images in Fig. 6; here, we can observe a small defect in the 113 habit plane. We have modeled substitutional elements C, B, and N to see if they have low segregation energy at this twin boundary. In addition, oxygen has been proposed as a possibility. However, the most likely scenario would be for interstitial segregation to occur. The gettering ability of a perfectly coherent  $\Sigma 3$  twin boundary has been reported to be weak and having very little interaction with impurities.<sup>44,50</sup> The oxygen has mostly been found to getter dislocations composed of small-angle tilt boundaries (SATBs) and has only been found to segregate to  $\Sigma 3$  twin boundaries if the boundary is connected with dislocations.<sup>51–53</sup> The gettering ability of oxygen atoms has been shown to depend both on the dislocation strain and on the dislocation density. Maji *et al.*<sup>54</sup> found that local tensile strain due to vacancies or geometrical distortions favors oxygen segregation at

$\Sigma 3$  twin boundaries. The defect observed in Figs. 6 and 7 could be due to precipitates decorating a small defect and due to a small tilt in orientation between the two grains. The contrast differences in the HRTEM images could imply that this is an initial stage of a coherent precipitate disk called a Guinier–Preston zone (GP zone)<sup>55</sup> often found in metallic alloys. Similar precipitates have been observed by Ohno *et al.*,<sup>56</sup> where Cu precipitation is formed in a similar process as GP-zones were observed at small-angle tilt boundaries. Duguay *et al.*<sup>57</sup> investigated silicon doped with high amounts of boron and found a high density of dislocation loops and enriched rods as 113 defects. Similar defects have been in other materials, such as electron-irradiated Ge investigated by Lima and Howie,<sup>58</sup> where small rod-like 113 defects were observed. However, more investigations are needed to confirm the metallic impurities.

## V. CONCLUSION

In this paper, we have investigated the underlying reasons for the HSPL VID3 band emission peak in multicrystalline silicon by hyperspectral imaging, SEM, EBSD, and STEM. The results have shown that the location of the VID3 peak intensity is at

1. the area with high grain reference orientation deviation (high GROD angle),
2. at the sub-grain boundary or near the  $\Sigma 3$  twin boundary, and
3. defects near the  $\Sigma 3$  twin boundary, which may be caused by a defect in another plane, precipitates decorating a small defect, or a tilt deviation between two grains,

where one or more of these conditions should be present for the HSPL VID3 band emission peak to be intense.

## ACKNOWLEDGMENTS

This work was funded by the Research Council of Norway through the funding program EnergiX, for the project “LeTID in



multicrystalline PERC cells” (LetUP) (No. 280909). The Research Council of Norway is also acknowledged for the support to The Norwegian Transmission Electron Microscopy Centre (No. 197405).

## AUTHOR DECLARATIONS

### Conflict of Interest

The authors have no conflicts to disclose.

## DATA AVAILABILITY

The data that support the findings of this study are available from the corresponding author upon reasonable request.

## REFERENCES

- <sup>1</sup>A. Flø, I. Burud, K. Kvaal, R. Søndena, and E. Olsen, *AIP Adv.* **3**, 112120 (2013).
- <sup>2</sup>S. J. Pearton, J. W. Corbett, and M. Stavola, *Hydrogen in Crystalline Semiconductors* (Springer-Verlag, Heidelberg, 1992).
- <sup>3</sup>B. Sopori, Y. Zhang, and N. M. Ravindra, *J. Electron. Mater.* **30**, 1616–1627 (2001).
- <sup>4</sup>L. J. G. A. Azzizi and D. H. Macdonald, in *Proceedings 19th EU PVSEC* (WIP, Paris, 2004).
- <sup>5</sup>B. J. Hallam, P. G. Hamer, S. Wang, L. Song, N. Nampalli, M. D. Abbott, C. E. Chan, D. Lu, A. M. Wenham, L. Mai *et al.*, *Energy Procedia* **77**, 799 (2015).
- <sup>6</sup>M. S. Wiig, H. Haug, R. Søndena, and E. S. Marstein, *Energy Procedia* **124**, 215 (2017).
- <sup>7</sup>H. Haug, M. S. Wiig, R. Søndena, B. Rynningen, G. Stokkan, and Ø. Mjos, in *36th EUPVSEC* (WIP, Marseille, 2019).
- <sup>8</sup>B. J. Hallam, P. G. Hamer, A. M. Ciesla née Wenham, C. E. Chan, B. Vicari Stefani, and S. Wenham, *Prog. Photovoltaics Res. Appl.* **28**, 1217 (2020).
- <sup>9</sup>K. Adamczyk, R. Søndena, G. Stokkan, E. Looney, M. Jensen, B. Lai, M. Rinio, and M. Di Sabatino, *J. Appl. Phys.* **123**, 055705 (2018).
- <sup>10</sup>N. A. Drozdov, A. A. Patrin, and V. D. Tkachev, *Sov. Phys. JETP Lett.* **23**, 597 (1976), [http://jetpletters.ru/ps/1806/article\\_27602.shtml](http://jetpletters.ru/ps/1806/article_27602.shtml).
- <sup>11</sup>S. Pizzini, M. Guzzi, E. Grilli, and G. Borionetti, *J. Phys.: Condens. Matter* **12**, 10131 (2000).
- <sup>12</sup>R. Sauer, J. Weber, J. Stolz, E. R. Weber, K. H. Kusters, and H. Alexander, *Appl. Phys. A* **36**, 1 (1985).
- <sup>13</sup>T. Mehl, I. Burud, E. Letty, and E. Olsen, *Energy Procedia* **124**, 107 (2017).
- <sup>14</sup>G. M. Wyller, F. Schindler, W. Kwapiel, J. Schön, E. Olsen, H. Haug, S. Riepe, and M. C. Schubert, *IEEE J. Photovoltaics* **9**, 55 (2019).
- <sup>15</sup>M. Tajima, Y. Iwata, F. Okayama, H. Toyota, H. Onodera, and T. Sekiguchi, *J. Appl. Phys.* **111**, 113523 (2012).
- <sup>16</sup>E. C. Lightowers and V. Higgs, *Phys. Status Solidi A* **138**, 665 (1993).
- <sup>17</sup>H. T. Nguyen, M. A. Jensen, L. Li, C. Samundsett, H. C. Sio, B. Lai, T. Buonassisi, and D. Macdonald, *IEEE J. Photovoltaics* **7**, 772 (2017).
- <sup>18</sup>M. Tajima, *IEEE J. Photovoltaics* **4**, 1452 (2014).
- <sup>19</sup>D. Lausch, T. Mehl, K. Petter, A. Svarstad Flø, I. Burud, and E. Olsen, *J. Appl. Phys.* **119**, 054501 (2016).
- <sup>20</sup>H. T. Nguyen, F. E. Rougieux, F. Wang, H. Tan, and D. Macdonald, *IEEE J. Photovoltaics* **5**, 799 (2015).
- <sup>21</sup>T. Sekiguchi and K. Sumino, *J. Appl. Phys.* **79**, 3253 (1996).
- <sup>22</sup>M. Syre, S. Karazhanov, B. R. Olaisen, A. Holt, and B. G. Svensson, *J. Appl. Phys.* **110**, 024912 (2011).
- <sup>23</sup>P. M. Weiser, E. Monakhov, H. Haug, M. S. Wiig, and R. Søndena, *J. Appl. Phys.* **127**, 065703 (2020).
- <sup>24</sup>H. Haug, R. Søndena, M. S. Wiig, and E. S. Marstein, *Energy Procedia* **124**, 47 (2017).
- <sup>25</sup>E. Olsen and A. Flø, *Appl. Phys. Lett.* **99**, 011903 (2011).
- <sup>26</sup>D. Lausch, M. Gläser, and C. Hagendorf, *J. Appl. Phys.* **114**, 194509 (2013).
- <sup>27</sup>R. Tauler, *Chemom. Intell. Lab. Syst.* **30**, 133 (1995).
- <sup>28</sup>C. T. Koch, see [https://www.physics.hu-berlin.de/en/sem/software/software\\_fwrttools](https://www.physics.hu-berlin.de/en/sem/software/software_fwrttools) for FRWRtools plugin.
- <sup>29</sup>G. Kresse and J. Furthmüller, *Phys. Rev. B* **54**, 11169 (1996).
- <sup>30</sup>G. Kresse and J. Furthmüller, *Comput. Mater. Sci.* **6**, 15 (1996).
- <sup>31</sup>J. P. Perdew and Y. Wang, *Phys. Rev. B* **46**, 12947 (1992).
- <sup>32</sup>C. Haase, M. Kühbach, L. A. Barrales-Mora, S. L. Wong, F. Roters, D. A. Molodov, and G. Gottstein, *Acta Mater.* **100**, 155 (2015).
- <sup>33</sup>H. Wang, N. Usami, K. Fujiwara, K. Kutsukake, and K. Nakajima, *Acta Mater.* **57**, 3268 (2009).
- <sup>34</sup>P. Pumphrey and K. Bowkett, *Scr. Metall.* **5**, 365 (1971).
- <sup>35</sup>D. P. Stadelmann, see <https://www.jems-swiss.ch/> for JEMS-SWISS.
- <sup>36</sup>R. Maji, E. Luppi, N. Capron, and E. Degoli, *Acta Mater.* **204**, 116477 (2021).
- <sup>37</sup>V. Oliveira, B. Marie, C. Cayron, M. Marinova, M. Tsoutsouva, H. Sio, L. Lafford, J. Baruchel, G. Audoit, A. Grenier *et al.*, *Acta Mater.* **121**, 24 (2016).
- <sup>38</sup>G. Stokkan, *J. Cryst. Growth* **384**, 107 (2013).
- <sup>39</sup>J. Chen, T. Sekiguchi, D. Yang, F. Yin, K. Kido, and S. Tsurekawa, *J. Appl. Phys.* **96**, 5490 (2004).
- <sup>40</sup>T. Duffar, *Recent Res. Dev. Cryst. Growth* **5**, 61 (2010); see <https://hal.archives-ouvertes.fr/hal-00456228>.
- <sup>41</sup>A. Bary and G. Nouet, *J. Appl. Phys.* **63**, 435 (1988).
- <sup>42</sup>G. Sarau, S. Christiansen, M. Holla, and W. Seifert, *Sol. Energy Mater. Sol. Cells* **95**, 2264 (2011).
- <sup>43</sup>T. Buonassisi, A. A. Istratov, M. D. Pickett, M. A. Marcus, T. F. Ciszek, and E. R. Weber, *Appl. Phys. Lett.* **89**, 042102 (2006).
- <sup>44</sup>A. Stoffers, O. Cojocaru-Mirédin, W. Seifert, S. Zaefferer, S. Riepe, and D. Raabe, *Prog. Photovoltaics Res. Appl.* **23**, 1742 (2015).
- <sup>45</sup>Y. Ohno, T. Tamaoka, H. Yoshida, Y. Shimizu, K. Kutsukake, Y. Nagai, and N. Usami, *Appl. Phys. Express* **14**, 011002 (2020).
- <sup>46</sup>G. Stokkan, Y. Hu, O. Mjos, and M. Juel, *Sol. Energy Mater. Sol. Cells* **130**, 679 (2014).
- <sup>47</sup>A. Paxton and A. Sutton, *Acta Metall.* **37**, 1693 (1989).
- <sup>48</sup>K. Kutsukake, N. Usami, T. Ohtaniuchi, K. Fujiwara, and K. Nakajima, *J. Appl. Phys.* **105**, 044909 (2009).
- <sup>49</sup>P. A. Carvalho, A. Thøgersen, Q. Ma, D. N. Wright, S. Diplas, A. Galeckas, A. Azarov, V. Jokubavicius, J. Sun, M. Syväjärvi *et al.*, *SciPost Phys.* **5**, 21 (2018).
- <sup>50</sup>Y. Ohno, K. Inoue, Y. Tokumoto, K. Kutsukake, I. Yonenaga, N. Ebisawa, H. Takamizawa, Y. Shimizu, K. Inoue, Y. Nagai *et al.*, *Appl. Phys. Lett.* **103**, 102102 (2013).
- <sup>51</sup>Y. Ohno, K. Inoue, K. Fujiwara, M. Deura, K. Kutsukake, I. Yonenaga, Y. Shimizu, K. Inoue, N. Ebisawa, and Y. Nagai, *Appl. Phys. Lett.* **106**, 251603 (2015).
- <sup>52</sup>Y. Ohno, K. Inoue, K. Fujiwara, K. Kutsukake, M. Deura, I. Yonenaga, N. Ebisawa, Y. Shimizu, K. Inoue, Y. Nagai *et al.*, *Appl. Phys. Lett.* **110**, 062105 (2017).
- <sup>53</sup>Y. Ohno, K. Kutsukake, M. Deura, I. Yonenaga, Y. Shimizu, N. Ebisawa, K. Inoue, Y. Nagai, H. Yoshida, and S. Takeda, *Appl. Phys. Lett.* **109**, 142105 (2016).
- <sup>54</sup>R. Maji, E. Luppi, N. Capron, and E. Degoli, *Acta Mater.* **204**, 116477 (2021).
- <sup>55</sup>G. Preston, *Nature* **142**, 570 (1938).
- <sup>56</sup>Y. Ohno, K. Inoue, K. Kutsukake, M. Deura, T. Ohsawa, I. Yonenaga, H. Yoshida, S. Takeda, R. Taniguchi, H. Otubo *et al.*, *Phys. Rev. B* **91**, 235315 (2015).
- <sup>57</sup>S. Duguay, T. Philippe, F. Cristiano, and D. Blavette, *Appl. Phys. Lett.* **97**, 242104 (2010).
- <sup>58</sup>C. A. F. Lima and A. Howie, *Philos. Mag.* **34**, 1057 (1976).